Available online at www.sciencedirect.com

SciVerse ScienceDirect

Ceramics International 38 (2012) 2873–2882

CERAMICS INTERNATIONAL

www.elsevier.com/locate/ceramint

Synthesis of WO_3 thin films by surfactant mediated spray pyrolysis

L.M. Bertus, A. Duta *

Department of Renewable Energy Systems and Recycling, Transilvania University of Brasov, Eroilor 29, 500036 Brasov, Romania

Received 6 October 2011; received in revised form 14 November 2011; accepted 22 November 2011
Available online 29 November 2011

Abstract

WO_3 thin films were prepared by surfactant mediated spray pyrolysis deposition on fluorine-doped tin oxide (FTO) conductive glass using hexadecylthymethylammonium bromide (HTAB) as structure-directing agent. The crystalline structure, topography, electrical conductivity and optical properties were investigated as function of cationic surfactant concentration. High transparency and conductivity were obtained for the sample which contained the lowest amount of surfactant (50 ppm) in the spraying solution. Significant changes in the morphology were observed with increasing HTAB addition level; samples lost their homogeneity and porosity, while the layer roughness increased. The surfactant by-products resulted after annealing were investigated based on FTIR analysis and a decomposition scheme was proposed. The modified surface composition and morphology influenced the hydrophilic character of the samples.

Keywords: B. Surfaces; C. Electrical properties; C. Optical properties; WO_3 thin films; Surfactant mediated spray pyrolysis

1. Introduction

Mesoporous tungsten oxide (WO_3) is the most promising candidate for electrochromic [1] and gas sensing materials [2]. Literature contains many reports confirming that the optical and the electrical properties of WO_3 are closely related to its level of crystallization and to the surface morphology [3,4].

One of the major challenges in obtaining nanostructured materials is to control the crystalline structure and morphology of the films, tailoring polymorphism, porosity, grain size and the grain boundaries.

WO_3 thin films have been synthesized by processes involving physical transformation, here including physical vapor deposition (PVD) [5], sputtering [6,7] and evaporation [8,9], and also by using techniques based on chemical processes occurring either in the gas phase such as chemical vapor deposition (CVD) [10,11] or in solution including electrodeposition [12], anodization [13], sol–gel deposition [14,15] and spray pyrolysis.

Although physical methods have the advantage of excellent control over the layer stoichiometry and interface, the wet chemical routes offer better reproducibility and control in terms of crystallinity, thickness and porosity and flexibility in choosing the type of substrate or precursor. Spray pyrolysis is a versatile deposition method because apart all the above mentioned advantages it allows the use of inexpensive precursor materials and large-area coatings can be obtained by using low-cost equipments with minimum energy consumption.

During the SPD process, a precursor solution is atomized and resulting aerosols are sprayed toward a heated substrate. Ideally the solvent evaporates completely close to the substrate where the reactant molecules undergo chemical reaction which leads to nucleation and layer growth.

For obtaining WO_3 thin films by SPD different precursor solutions were prepared including aqueous solutions of ammonium tungstate ($(NH_4)_2WO_4$) [16–19] and peroxotungstate [20], WCl_6 dissolved in N,N-dimethyl formamide [21] or in a mixture of ethanol:water (50:50%) [22] and also $W(OC_2H_5)_6$ ethanolic solutions [23,24].

Deposition temperature and precursor solution concentration are the main technological parameters that influence the nucleation and crystal growth processes and thus the deposition rate, thickness and uniformity of the films synthesized by SPD. The precursor type influences the solvent evaporation rate within the aerosol droplets and the droplets speed up through modification of superficial tension.

So, one way of controlling the nucleation and growth processes is using surfactants which act as growth controlling

---

* Corresponding author. Tel.: +40 723561089.
E-mail address: a.duta@unitbv.com (A. Duta).

0272-8842/$36.00 © 2011 Elsevier Ltd and Techna Group S.r.l. All rights reserved.
doi:10.1016/j.ceramint.2011.11.060

agents, as well as agglomeration inhibitors. Ordered arrangements of particulates directed by surfactant self-assemblies are formed, followed by template removal by extraction or calcinations. Because of their amphilic nature, the surfactant molecules can form different types of aggregate structures in the solution, such as spherical, cylindrical, cubic, hexagonal and lamellar phases, therefore the morphology of the surfactant template directly determines the pore structure of the nanolayers.

Extensive research has been carried out on the template-assisted production of WO_3 layers using cationic surfactants such as hexadecylthymethylammonium bromide (HTAB) [25,26], anionic surfactants including sodium dodecyl sulfate (SDS) [4], as well as nonionic surfactants including poly(alkylene oxide) triblock copolymers such as L62 and P123 [27,28], lyotropic liquid crystals such as Brij 35 and Brij 56 [29,30] and various biodegradable surfactants [31]. However when using organic templates the structure can shrink and the crystallographic order and layer homogeneity might be lost after organic phase removal by calcination, damaging the optical and the electrical properties of the layers.

In this paper we report for the first time the synthesis of WO_3 thin layers by spray pyrolysis using as precursor an ethanolic solution of WCl_6 containing a cationic surfactant (hexadecylthymethylammonium bromide, HTAB) as structure directing agent.

The effect of the HTAB concentration on the structure and morphology of the WO_3 layers and their correlation with the electrical and optical properties were investigated, aiming to develop novel solutions applicable in electrochromic windows. The changes in the interface physical and chemical properties of the WO_3 thin layers and their influence on the opto-electronic response were investigated by correlating the crystalline structure (XRD), composition (FTIR), surface charge (contact angle measurement) and morphology (AFM) with the values of the contact angle.

2. Layer preparation and characterization

2.1. Deposition parameters

The WO_3 thin layers were deposited onto electrical conducting fluorine-doped tin oxide (FTO, Pilkington) using the spray pyrolysis technique. The precursor solution was obtained by dissolving 1.2 g WCl_6 (99.9+%, Acrős Organics) in ethanol (C_2H_5OH, 99.2%, P.A.M. Corporation S.R.L.) which contained 1 mL of acetyl acetone (99%, Alfa Aesar). Hexadecylthymethylammonium bromide (HTAB—$(C_{16}H_{33})N(CH_3)_3Br$, 98%, Alfa Aesar) was added to the previously obtained solution in different concentrations: 50, 200, 500 and 1000 ppm. Samples were denoted as WH50, WH200, WH500 and WH1000, respectively. Clean 2.5 cm × 2.5 cm FTO substrates were obtained after degreasing with pH neutral detergent, rinsed with deionized water and ultrasonically cleaned in ethanol, followed by drying in compressed air flow. During deposition, air was used as carrier gas ($P_{air} = 1$ bar) and the substrate temperature was maintained at 200 °C. The samples were annealed for 6 h, at 350 °C for stabilizing the crystalline structure and to remove the surfactant template.

2.2. Film characterization

The effect of the HTAB concentration on the crystal structure and on the surface morphology was investigated using X-ray diffraction (Advanced D8 Discover Bruker diffractometer, $Cu_{k\alpha 1}$ radiation, $\lambda = 0.15406$ nm) and atomic force microscopy (NT-MDT model NTGRA PRIMA EC, semicontact mode with Si-tips, NSG10, force constant 0.15 N/m, tip radius 10 nm). Variation in the semiconducting behavior was studied by current–voltage measurements (Princeton Applied Research VSP potentiostat/galvanostat). Transmittance spectra of the WO_3 samples with variable HTAB content were recorded by UV–vis spectrometry (Perkin Elmer Lambda 25) and used further in the calculation of the refractive index, absorption coefficient, extinction coefficient and layer thickness.

The static contact angle (θ) was measured by the sessile drop method, at constant room temperature (20 °C) using the OCA-20 Contact Angle-meter (DataPhysics Instruments). Two testing liquids with different polarity and surface tension (σ_{LV}) were used: glycerol ($\sigma_{L,V}^{20\,^{\circ}\mathrm{C}} = 63.40\,\mathrm{mN/m}$) and deionized water ($\sigma_{L,V}^{20\,^{\circ}\mathrm{C}} = 72.80\,\mathrm{mN/m}$). Contact angle measurement is a very sensitive method to surface modifications, however it does not provide information about the type of the surface groups. Thus, the functional groups located at the surface were investigated using a Spectrum BX FT-IR System (Perkin Elmer).

3. Results and discussions

3.1. Critical micelle concentration evaluation

The critical micelle concentration (CMC) is influenced by a number of factors including the nature of the surfactant, temperature, solvent/dispersion medium and the ionic solutes in the system. The properties of the aqueous solvents, such as temperature, pH and ionic strength influence the micelle formation, by this meaning their shape, size and stability. Therefore, the critical micelle concentration (CMC) of HTAB was investigated in water, ethanol and in ethanol with 100 ppm of WCl_6 powder and plots are presented in Fig. 1. Experiments were carried out by adding different amounts of a stock surfactant solution to a fixed volume of aqueous or alcoholic solution, followed by intensive stirring and conductivity measurements (Hanna HI 991300 conductometer) at 25 °C.

By modifying the surfactant concentration, the HTAB electrical conductivity (Fig. 1) in aqueous or alcoholic media presents two different regimes, corresponding to the behavior above and below the surfactant's critical micelle concentration. The CMC of HTAB was calculated at the intersection of the slopes corresponding to these two regimes.

The CMC of HTAB in aqueous media (293.72 ppm) is in good agreement with the reported values [32–34] confirming the reliability of the conductivity method. At low concentrations, in bulk solution, surfactants mainly exist

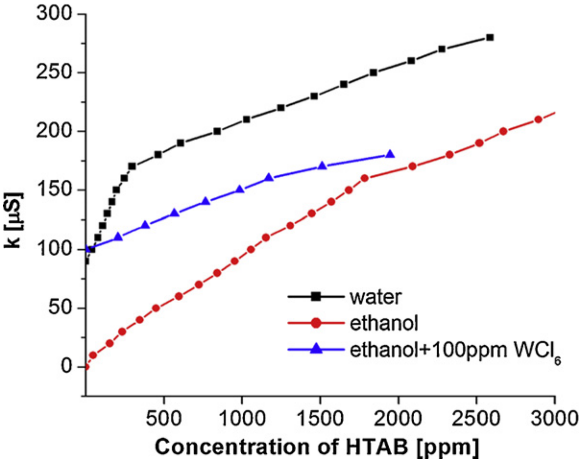

Fig. 1. Critical micelle concentration evaluation of HTAB in different media.

in monomer-like form. Above CMC the HTAB forms oil/water (O/W) type micelles.

The micellization point of HTAB in ethanol media was found to be much higher (1602.33 ppm) compared to water. Li et al. [34] also reported that the CMC of HTAB increased with increasing ethanol concentration in the mixed water–ethanol system. They proved that HTAB tail groups interact much stronger with ethanol comparing with water thus, the micelles are more difficult to form in ethanol (at higher concentrations). Ethanol may reduce the hydration of the micelle surface through hydrogen bonding within the palisade layer (see Scheme 1, ethanol section), increasing the electrostatic repulsive forces between the ionic head groups because of the increase in the charge density of micelle surface, preventing the surfactant molecules to associate.

By adding 100 ppm of WCl_6, a slight decrease of the CMC is registered (1176 ppm). It is well known that WCl_6 dissolves in ethanol by forming an ethoxy or ethoxy chloride complex (Eq. (1)) through partial or total replacement of the Cl^- anions with ethoxy ($C_2H_5O^-$). The micelle surface is positively charged due to the trimethylammonium head groups of the surfactant monomers (Scheme 1, ethanol–WCl_6 section) therefore, its properties are mainly affected by the salt anions. Because ethanol increases the charge density at the micelle surface, the Cl^- binding is favored. So, adding WCl_6 reduces the electrostatic repulsion between the charged groups by forming a *Stern* type layer at the micelle surface and favoring the aggregation process. These effects were previously reported by Jakubowska [33] who registered a decrease in the CMC value after adding KCl to HTAB aqueous systems

$$WCl_6 + xC_2H_5OH \rightarrow WCl_{6-x}(OC_2H_5)_x + xHCl \qquad (1)$$

Above CMC, surfactants can ‘‘trap’’ the precursor cation in the micelle (external) layers and modify their reactivity; supplementary, two effects are expected, related to (1) preventing the particle agglomeration and (2) acting as structure directing agent. Below CMC, the surfactant molecules are mainly dissolved and/or form a loose layer at the system's surface but it is also expected to group around the cation and change the nucleation rate. Therefore, HTAB was added in concentration lower (50, 200 and 500 ppm) and near (1000 ppm) the CMC in the alcohol–WCl_6 system. It is also to note that high amounts of surfactant may leave traces of carbon, even after annealing, altering the electrical properties of the film.

3.2. Structure, composition and morphology characterization

3.2.1. Crystalline structure

The as-deposited layers were amorphous, therefore annealing was applied to all the samples. The XRD spectra of the samples after annealing at 350 °C are presented in Fig. 2. The diffraction analysis show that only WH50 sample contains crystalline WO_3, with peaks corresponding to a mixture of two monoclinic phases according to JCPDS 87-2399 and JCPDS 83-0951. The spectra of the WH50 and WH200 samples also display peaks due to the FTO crystalline substrate.

With increasing surfactant content in the precursor solution, the peaks corresponding to crystalline WO_3 gradually disappear. For WH200 sample only peaks corresponding to

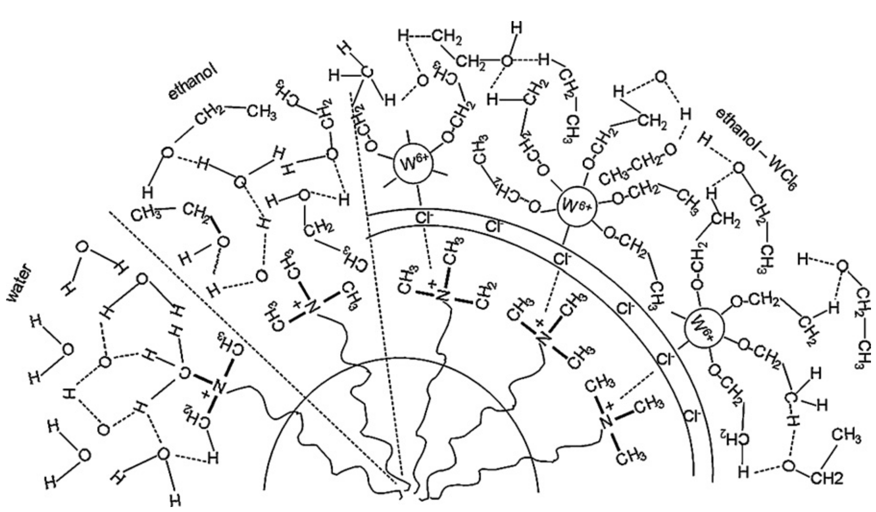

Scheme 1. Micelle dissolution of water, ethanol and ethanol–WCl_6.

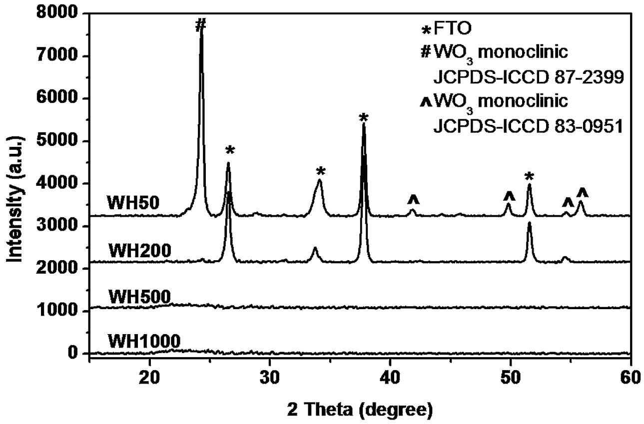

Fig. 2. XRD spectra of WH50, WH200, WH500 and WH100 samples after annealing at 350 °C.

FTO and a fading peak at $2\theta \sim 55^\circ$ corresponding to WO_3 monoclinic JCPDS 83-0951 are observed, whereas for WH500 and WH100 samples no peaks are observed, not even from the substrate, proving that a thick layer was developed probably consisting of amorphous WO_3.

3.2.2. *Fourier transform infra-red (FTIR) analysis*

The FTIR spectra of the samples annealed at 350 °C and that of HTAB in the 600–4000 cm^{-1} range are presented in Fig. 3. The representative bands for HTAB [35] are observed at 2846 and 2921 cm^{-1} corresponding to $\upsilon_s CH_2$ and $\upsilon_{as} CH_2$ symmetric and asymmetric stretching vibrations, respectively, and also at 1408, 1483, 1490 and 3015 cm^{-1} corresponding to $\delta_s CH_3$, $\delta_{as} CH_3$ and superimposed $\upsilon_s CH_3$ and $\upsilon_{as} CH_3$ vibrations of the $-N(CH_3)_3$ surfactant head groups.

The bands centered at 794 and 715 cm^{-1} are specific for crystalline WO_3 (m-phase), and correspond to the stretching vibrations of the bridging oxygen and these are assigned to W–O stretching (υ), W–O bending (δ) and O–W–O deformation (γ) modes, respectively [36,37]. With increasing surfactant content these bands are shifted to lower wave numbers (i.e. 783, 685 and 655 cm^{-1}). Similar bands at 784 cm^{-1} and 655 cm^{-1} were assigned to υ(W–O$_{intra}$–W) bridging stretch [4], and to υ(W–O–W) and υ_S(W–O–O) vibrations [38], respectively.

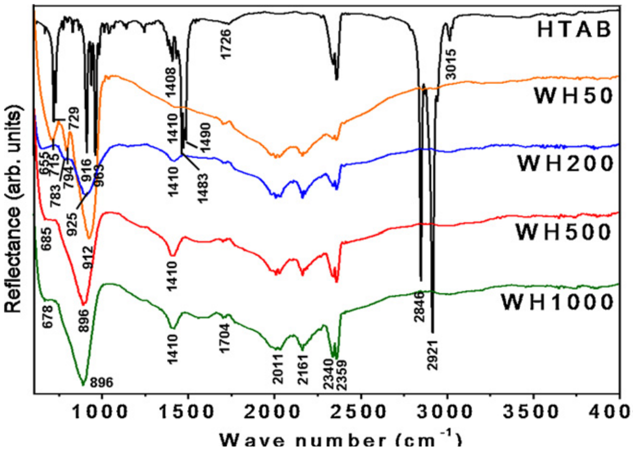

Fig. 3. FTIR spectra of HTAB and of WH50, WH200, WH500 and WH1000 samples.

The band at 912 cm^{-1} in WH50 sample is assigned by us to the υ(O–O) vibration and is shifted to 925 cm^{-1} in WH200 sample and to 896 cm^{-1} in WH500 and WH1000 samples. This band has earlier been observed at 900 cm^{-1} [39] and at 898 cm^{-1} [40] by Deepa who allocated it to the mixed contributions of the peroxo (υ(O–O)) and υ(W–O$_{inter}$–W) stretching vibrations of the bridging oxygen. The appearance of the bands characteristic to peroxo complexes starting with WH200 sample and the disappearance of the W=O vibration characteristic peaks in m-WO_3 are related to the crystallinity loss, as confirmed by XRD analysis. The shifts in the bands wave numbers are attributed to the changes in the film structure and composition, i.e. loss of the crystalline symmetry and stoichiometry due to organic by-product contamination, originating from the incomplete removal of the surfactant after annealing.

Characteristic bands of N,N-dimethyl formamide (DMF) are also identified in WH50, WH200, WH500 and WH1000 samples: a band at 1704 cm^{-1} mainly related to υ(C=O) stretching mode, another at 1410 cm^{-1} which is assigned to the scissoring δ(N–CH_3) mode of the $N(CH_3)_2$ group, and a large band between 1100 and 1300 cm^{-1} υ(C–H) corresponding to the vibrations resulted from the in-phase combination of υ(C–N) stretching and δ(C=O) bending vibration. The band at 1410 cm^{-1} is not so pronounced in WH50 sample but increases in intensity with increasing surfactant content.

Based on these data, we propose the following mechanism for the surfactant (HTAB) removal by calcination (Scheme 2): firstly, trimethylamine $[N(CH_3)_3]$ is formed through Hofmann elimination along with the corresponding alkene most probably during deposition when the precursor solution reaches the

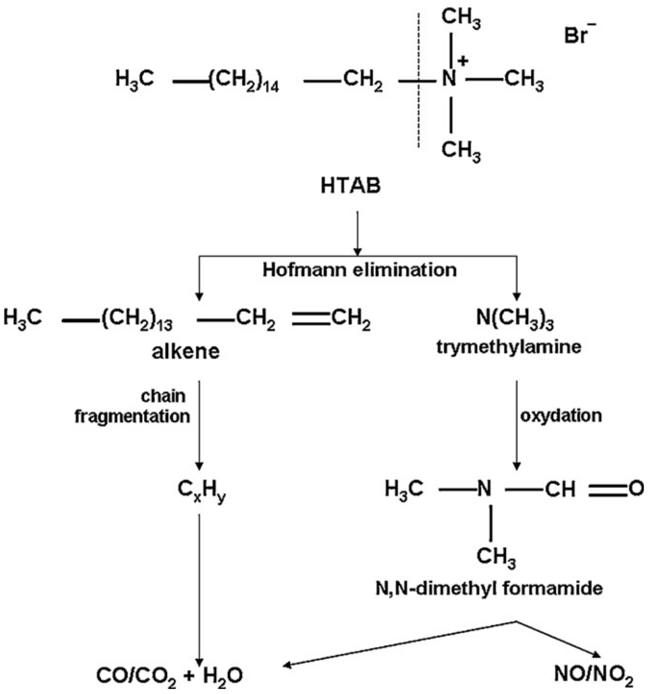

Scheme 2. Proposed mechanism for HTAB decomposition.

substrate heated at 200 °C. During annealing in air, N,N-dimethyl formamide is formed by trimethylamine oxidation. No bands are observed for the alkene probably because chain fragmentation occurred and the hydrocarbon species (C_xH_y) were decomposed to CO/CO_2 and H_2O. The vibrations at 2340 and 2359 cm^{-1} are attributed to the P branch and the R branch of the $\upsilon_{as}(\mathrm{O{=}C{=}O})$ antisymmetric stretching vibration, respectively [39]. Bands related to carbon monoxide are present also at 2011 cm^{-1} and 2161 cm^{-1} corresponding to the P branch and the R branch of the $\upsilon(\mathrm{CO})$ stretching vibrations, respectively [39]. The large band centered at c.a. 1580 cm^{-1} for the WH500 sample and its intensification for WH1000 sample was attributed by us to the superimposed $\upsilon_{as}(\mathrm{N{=}O})$ asymmetric and $\upsilon_{s}(\mathrm{N{=}O})$ symmetric stretching vibrations of NO or NO_2, confirming our mechanisms.

3.2.3. AFM analysis

As it can be seen from AFM images (Fig. 4), with increasing the HTAB concentration, the morphology of the samples becomes more flatten. Also, the average roughness, evaluated with AFM software over a 5 μm × 5 μm area and presented in Table 1, shows an increase with the surfactant content.

A dense granular morphology with relatively uniform distribution of grains characterizes the surface of the thin film in the WH50 sample. Grain boundaries possibly originate in those regions earlier occupied by HTAB before its removal through annealing and structural reorganization can be expected. We believe that the addition of the surfactant lowered the solution surface tension and increased the aerosol flow rate, and as s a result smaller droplets and greater in number were obtained which after reaching the substrate and the solvent was evaporated, allowed the uniform distribution of nucleation sites on the substrate thus explaining the homogenous growth of the layer WH50.

For the WH200 sample grains of irregular shape, sizes and orientations are formed, randomly distributed on the surface. No clear distinction between grains and grain boundaries can be made and this feature is even more accentuated for WH500 sample. Homogeneity and most importantly the apparent porosity of the layers prepared with higher concentration of surfactant decreased significantly. At higher concentration of HTAB in the spraying solution a high number of droplets is directed toward the substrate with too much speed so droplets splashing onto the substrate but also incomplete removal of the solvent cause non-uniform distribution of nucleation sites on the substrate and possibly large stable aggregate formation, which along with the uneven evaporation of the solvent produces rough non-uniform layers. Particle coalescence through annealing can also be responsible for this irregular morphology of the WH200 and WH500 layers.

The AFM image of WH1000 sample reveals a nonporous surface with cracks resulted during annealing probably caused by thermal stress originating from uncontrolled evaporation/decomposition of the solvent/surfactant molecules [41].

When adding a polymeric intermediate carrier gas pressure and pause between spraying sequences are two parameters that need to be carefully selected to allow solvent evaporation before reaching the substrate and by-products to evaporate from the film before the next layer is sprayed. For too small gaps between spraying sequences the film remains contaminated with solvent and surfactant by-products which accumulate in the profundity of the film with each spraying sequence having

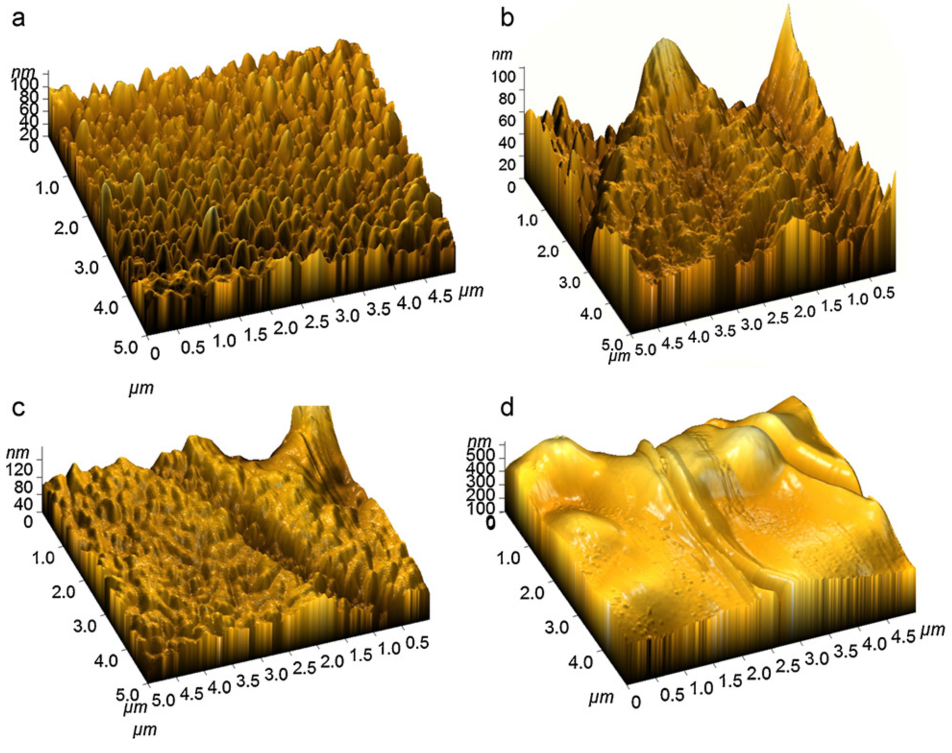

Fig. 4. AFM 3D topographies (5 μm × 5 μm) of the WH50 (a), WH200 (b), WH500 (c) and WH1000 (d) samples.

Table 1
Average roughness, layer thickness, average refractive index, packing density and band gap values of the samples.

Sample	Average roughness (nm)	Average refractive index ($\bar{n}$)	λ_1	λ_2	Layer thickness, d (nm)	Packing density (P)	Band gap, E_g (eV)
WH50	7.88	1.7013	479	615	635.97	0.6082	2.67
WH200	8.21	1.7015	470	620	569.41	0.6084	2.74
WH500	12.80	1.7017	468	616	570.85	0.6085	2.72
WH1000	36.21	1.7019	465	613	563.91	0.6086	2.82

consequences on the film transparency and conductivity. Not even the applied thermal treatment, i.e. annealing temperature 350 °C and annealing time 6 h, was not enough for by-product elimination and crystallization of the layers as shown by XRD spectra.

These data support the assumption of a beneficial effect of the very low surfactant concentrations, while at concentrations close to CMC large stable aggregate are likely to form within the precursor system, with a very slow nucleation, explaining the high roughness values. The effect of low HTAB concentration is mostly related to the surface tension in the aerosol droplets, decreasing their average radius, and promoting nucleation on the substrate from very small islands, resulting in thin dense films.

3.3. Electrical and optical properties

The current–voltage measurements were done using a gold contact on the substrate (FTO), for applying voltage, and another placed on the WO_3 layer to register the current intensity. Thus, a Schottky contact was formed between the gold contacts and the WO_3 layer.

All the samples exhibit p-type semiconducting behavior (Fig. 5), with sample WH50 showing the highest forward conductivity (Fig. 5, inset). A metal/p-type semiconductor junction is rectifying when the work function of the semiconductor is higher compared to metal [42], condition which is complied by our WO_3 semiconducting layers (4.3–4.9 eV and 5.10 eV for WO_3 and Au, respectively [43]).

The n- to p-type inversion in WO_3 is likely to occur for highly porous layers which have high concentration of oxygen vacancies, when thermally treated in highly oxidizing atmosphere. During annealing the majority of oxygen vacancies are reduced generating positive holes (Eq. (2)); another possibility is that the oxygen atoms adsorb at the surface of WO_3 and yield a tungsten vacancy and six positive holes (Eq. (3)), supporting even more p-type conductivity.

$$V_O^{\bullet\bullet} + \frac{1}{2}O_2 \rightarrow O_O^X + 2h^{\bullet} \qquad (2)$$

$$\frac{1}{2}O_2 \rightarrow V_W^{6/} + O_O^X + 6h^{\bullet} \qquad (3)$$

The decrease in conductivity with increasing HTAB content in the spraying solution indicates that the annealing treatment did not completely remove the surfactant, leaving nonconducting amorphous species in the film, as confirmed by FTIR and XRD spectra. Also, looking at the AFM images (Fig. 4) we can see that the porosity of the surface layer decreases so we expect to have the lowest concentration of oxygen vacancies on the surface of the WH1000 sample, explaining the poor forward conductivity of this layer.

Considering that the use of WO_3 thin films targets mainly electrochromic applications, the optical properties were investigated. The optical transmittance of the samples for a wavelength range of 300–900 nm is presented in Fig. 6. The oscillations in the transmittance spectra are caused by optical interference arising from the difference between the refractive index of the WO_3 films and the substrate and also the interference of the multiple reflections of the film and substrate surfaces [44].

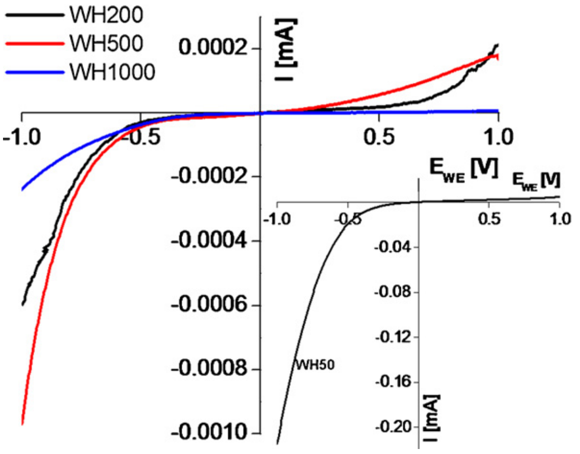

Fig. 5. *I–V* curves of samples as function of surfactant content.

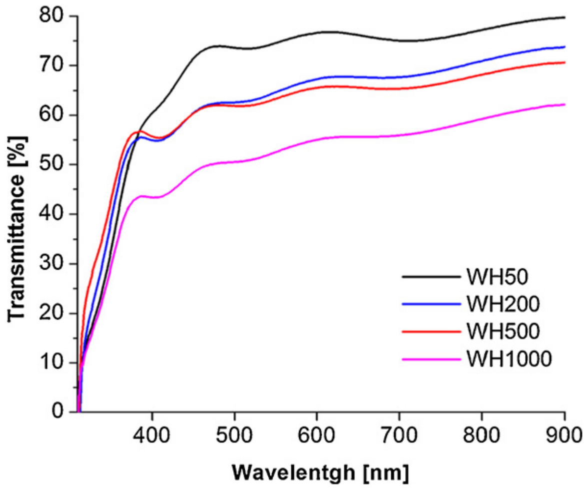

Fig. 6. Transmittance spectra of samples as function of surfactant (HTAB) content.

According to the envelope method elaborated by Swanepoel [45,46] the refractive index of a homogenous film can be calculated from transmission spectra in the medium and low absorbing region by using the interference fringes with the following formula (Eq. (4)):

$$n = [M + (M^2 - s^2)^{1/2}]^{1/2} \tag{4}$$

where M is

$$M = 2s\frac{T_M - T_m}{T_M \cdot T_m} + \frac{(s^2+1)}{2} \tag{5}$$

T_m and T_M are the maximum and minimum transmission values at a particular wavelength and s is the refractive index of the substrate (1.7). The average refractive index $(\bar{n})$ was calculated for the 430–900 wavelength range.

Using the refractive indices n_1 and n_2 of two adjacent maxima or minima calculated with the method described above, which correspond to the wavelengths λ_1 and λ_2, the thickness of the film (d) is calculated from the relation (6).

$$d = \frac{\lambda_1\lambda_2}{2(\lambda_1 n_2 - \lambda_2 n_1)} \tag{6}$$

Knowing the layer thickness (d) the absorption coefficient α and the extinction coefficient k can be obtained by the following formulae:

$$\alpha = \left(\frac{1}{d}\right)\ln(X), \tag{7}$$

$$k = \frac{\alpha\lambda}{4\pi}, \tag{8}$$

where

$$X = \frac{(n-1)(s-n)[1+(T_M/T_m)^{1/2}]}{(n+1)(s+n)[1-(T_M/T_m)^{1/2}]}. \tag{9}$$

The relative density is defined as the ratio of the densities of the film to that of the bulk. The packing density was calculated using the Lorentz–Lorentz formula (Eq. (10)) and the bulk refractive index of WO_3 at 550 nm is 2.5 [47]:

$$P = \frac{(s^2+1)(n^2-1)}{(s^2-1)(n^2+1)} \tag{10}$$

The average refractive index $(\bar{n})$ values, layer thicknesses and packing density of the samples are reported in Table 1. The variation of the absorption coefficient and extinction coefficient in the 430–900 nm wavelength range are presented in Fig. 7a and b, respectively.

The few and reduced amplitude interference fringes in the spectra reveal that all the WO_3 layers are not quite optically smooth surfaces [48]. The sharp slope in the transmittance spectra corresponds to the fundamental absorption edge of WO_3 and is blue shifted with increasing HTAB concentration up to the sample WH1000 when a red shift can be observed.

Transparency of the films decreases with increasing surfactant content, although layer thickness slightly decreases (Table 1), which could be attributed to the rising average roughness of the layers. High surface roughness values will increase surface optical scattering and optical loss [49,50] which explains the increasing values of the absorption and extinction coefficient. So, although layer WH1000 has the lowest thickness, absorption coefficient and extinction coefficient, it has the lowest transmission level because of the increased roughness (36.21 nm). Also the traces of by-products coming from surfactant decomposition might have a scattering effect because of the multiphase character of the surface. The values of the layer thickness, along with the results in the XRD and FTIR spectra support the assumption that a thick layer was formed for high concentration of HTAB which mainly consists of amorphous species. The WH50 layer has the highest transmittance, over 70%, as it is characterized by the lowest roughness (7.88 nm). These values fit well with the targeted applications.

As it can be seen from Table 1, the different compositions of the spraying solution do not induce significant changes in the mean refractive index. This confirms that the changes in the surface morphology showed by the AFM measurements are only in the superficial layer whereas the films packing density remains unchanged (Table 1).

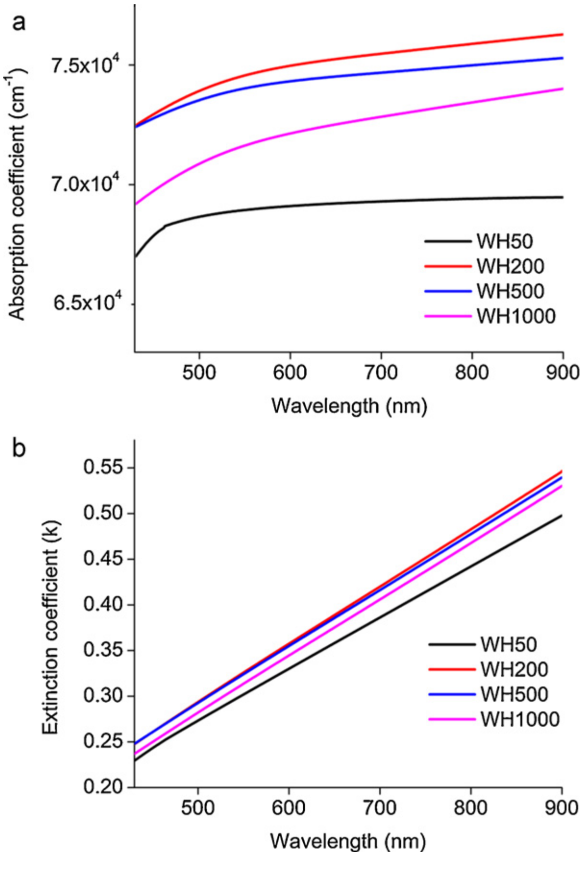

Fig. 7. Variations of the (a) absorption coefficient, *a*, and (b) extinction coefficient, *k*, with wavelength for WO_3 thin films.

Table 2
Results of contact angle measurement.

Sample	Contact angle θ (°)		Surface energy, σ_S (mN/m)	Dispersion component, σ^D (mN/m)	Polar component, σ^P (mN/m)	Surface polarity, χ^P
	Water	Glycerol				
WH50	63.26	80.88	59.35	0.21	59.14	0.99
WH200	42.96	79.69	124.00	8.59	115.42	0.93
WH500	49.46	75.40	87.33	1.67	85.66	0.98
WH1000	77.09	78.54	27.88	4.79	23.09	0.82

Using the transmittance spectra, the band gap was also evaluated using the relation:

$$\alpha h\upsilon = A(h\upsilon - E_g)^n \tag{11}$$

where A is a constant, $h\upsilon$ is the incident photon energy, E_g is the optical energy band gap, and α is the absorption coefficient. The exponent value was considered $n = 2$, as WO_3 is an indirect band gap semiconductor.

Band gap values of the samples are presented in Table 1. The increase in the band gap values can be associated with the decrease in the crystalline degree [51].

3.4. Contact angle measurements

The surface energy of the films is important considering the multi-layered applications involving the WO_3 thin layers and other possible applications in polar solvents.

The θ values recorded at the initial moment of the drop-film contact for water and glycerol are presented in Table 2. The contact angle depends on the relative surface free energy of the solid–liquid, solid–vapor, and liquid–vapor interfaces. The relation between interfacial interactions is described by Young's equation (12).

$$\sigma_{SL} = \sigma_S - \sigma_L \cos(\theta) \tag{12}$$

According to Owens–Wendt–Rabel and Kaelble method [52] one can separate the surface energies σ_S and σ_L into two interaction components: the dispersive part σ^D representing the van der Waals interaction and the polar part σ^P representing interactions between permanent dipoles and/or between permanent and induced dipoles. Surface free energies (σ_{SL}) and their dispersive (σ^D) and polar (σ^P) components were calculated by subtracting the geometric mean of both polar and dispersive contributions according to the Owens–Wendt–Rabel and Kaelble relationship:

$$\frac{(1+\cos\theta)\cdot\sigma_L}{2\sqrt{\sigma_L^D}} = \sqrt{\sigma_S^P\cdot\frac{\sigma_L^P}{\sigma_L^D}} + \sqrt{\sigma_S^D} \tag{13}$$

where σ_L^D and σ_L^P represent the dispersive and polar parts of the liquid, σ_S^D and σ_S^P represent the respective contributions of the solid and θ is the contact angle of testing liquid.

Surface polarity (χ^P) was calculated from the surface energy and its polar component using the following relation [53]:

$$\chi^P = \frac{\sigma^P}{\sigma} \tag{14}$$

The data in Table 2 summarizes the calculated surface energy of the samples with their dispersive and polar components and the surface polarity.

No significant changes are observed in the contact angles with glycerol, which has lower polarity, suggesting that WO_3 surface has predominantly ionic groups. It is well known that metal oxides exposed to the ambient environment adsorb water molecules, resulting in chemically equivalent metal hydroxyl groups (M–OH), explaining the hydrophilic character of WH50 sample. The higher surface OH density the higher the water contact angle is observed [54]. As the surfactant content increases part of the OH groups occupying the surface sites of the WO_3 layer are replaced by organic polar intermediaries originating from the surfactant decomposition, such as N,N-dimethyl formamide, as confirmed by FTIR spectra, becoming increasingly hydrophilic. A strong influence of the by-products resulted from the precursor thermal degradation on the surface polarity and thus on the water contact angle has been previously demonstrated in our group [55]. The WH200 sample has the lowest contact angle with water (the highest ionic degree), the highest surface energy and polar component, and consequently the highest wettability. This could be an important feature when targeting further applications as photo-catalysis. So we could relate the changes in morphology with the uptake of water from atmosphere during cooling of the samples, process which is favored by the presence of polar intermediates at the surface, such as N,N-dimethyl formamide (Scheme 2), which increase the hydrophilic character of the layers. The film deposited from micelles (WH1000) is much more inert, proving that surface roughness is less important comparing to the (very) small pores when predicting the physical and chemical interactions with water.

4. Conclusions

Tungsten oxide layers were obtained by spray pyrolysis of a precursor solution containing HTAB as structure directing agent in different concentrations (50, 200, 500 and 1000 ppm), selected considering the surfactant CMC in the WCl_6–ethanol system. Crystalline WO_3 with monoclinic structure was obtained for the sample with the lowest content of surfactant (WH50, 50 ppm HTAB) after annealing at 350 °C, whereas predominant amorphous structures were obtained for the other three samples. The highest transparency and conductivity were obtained for the crystalline WH50 sample which is characterized by a relatively uniform surface with reduced roughness.

Significant changes in the morphology are observed for the samples containing higher amounts of surfactant, ranging from a grain-like uniform morphology (WH50) to a rough flatten structure (WH1000). If added in high concentrations, surfactants can hinder crystal growth and possibly generate amorphous species within the structure which decrease the electrical conductivity.

The sample obtained using 50 ppm HTAB has optimal transmission properties in the visible part of the solar spectrum and convenient electrical conductivity, making it suitable for electrochromic windows applications.

Acknowledgements

This work was supported by the Sectoral Operational Programme Human Resources Development (SOP HRD), ID59321, financed from the European Social Fund and by the Romanian Government.

References

[1] C.G. Granqvist, Handbook of Inorganic Electrochromic Materials, Elsevier Science, Amsterdam, 1995.

[2] L.G. Teoh, Y.M. Hon, J. Sieh, W.H. Lay, M.H. Hon, Sensitivity properties of a novel NO_2 gas sensor based on mesoporous WO_3 thin film, Sens. Actuators B 96 (2003) 219.

[3] A.A. Joraid, S.N. Alamri, Effect of annealing on structural and optical properties of WO_3 thin films prepared by electron-beam coating, Physica B 391 (2007) 199.

[4] M. Deepa, A.K. Srivastava, S.A. Agnihotry, Influence of annealing on electrochromic performance of template assisted, electrochemically grown, nanostructured assembly of tungsten oxide, Acta Mater. 54 (2006) 4583.

[5] A. Subrahmanyam, A. Karuppasamy, Optical and electrochromic properties of oxygen sputtered tungsten oxide (WO_3) thin films, Sol. Energy Mater. Sol. Cells 91 (2007) 266.

[6] E. Washizu, A. Yamamoto, Y. Abe, M. Kawamura, K. Sasaki, Optical and electrochromic properties of RF reactively sputtered WO_3 films, Solid State Ionics 165 (2003) 175.

[7] M. Stankova, X. Vilanova, E. Llobet, J. Calderer, C. Bittencourt, J.J. Pireaux, X. Correig, Influence of the annealing and operating temperatures on the gas-sensing properties of RF sputtered WO_3 thin-film sensors, Sens. Actuators B: Chem. 105 (2005) 271.

[8] A.H. Jayatissa, S.T. Cheng, T. Gupta, Annealing effect on the formation of nanocrystals in thermally evaporated tungsten oxide thin films, Mater. Sci. Eng. B 109 (2004) 269.

[9] I. Porqueras, E. Bertran, Efficiency of Li doping on electrochromic WO_3 thin films, Thin Solid Films 377 (378) (2000) 129.

[10] R.E. Tanner, A. Szekeres, D. Gogova, K. Gesheva, Study of the surface roughness of CVD-tungsten oxide thin films, Appl. Surf. Sci. 218 (2003) 163.

[11] K.A. Gesheva, G. Popkirov, M. Ganchev, E. Tzvetkova, Electrochromic properties of atmospheric CVD MoO_3 and MoO_3–WO_3 films and their application in electrochromic devices, Mater. Sci. Eng. B 119 (2005) 232.

[12] R. Vijayalakshmi, M. Jayachandran, C. Sanjeeviraja, Structural, electrochromic and FT-IR studies on electrodeposited tungsten trioxide films, Curr. Appl. Phys. 3 (2003) 171.

[13] Y.S. Krasnov, G.Y. Kolbasov, Electrochromism and reversible changes in the position of fundamental absorption edge in cathodically deposited amorphous WO_3, Electrochim. Acta 49 (2004) 2425.

[14] M. Deepa, T.K. Saxena, D.P. Singh, K.N. Sood, S.A. Agnihotry, Spin coated versus dip coated electrochromic tungsten oxide films: structure, morphology, optical and electrochemical properties, Electrochim. Acta 51 (2006) 1974.

[15] A. Patra, K. Auddy, D. Ganguli, J. Livage, P.K. Biswas, Sol–gel electrochromic WO_3 coatings on glass, Mater. Lett. 58 (2004) 1059.

[16] R. Sivakumar, A. Moses Ezhil Raj, B. Subramanian, M. Jayachandran, D.C. Trivedi, C. Sanjeeviraja, Preparation and characterization of spray deposited n-type WO_3 thin films for electrochromic devices, Mater. Res. Bull. 39 (2004) 1479.

[17] S.R. Bathe, P.S. Patil, Titanium doping effects in electrochromic pulsed spray pyrolysed WO_3 thin films, Solid State Ionics 179 (2008) 314.

[18] A. Enesca, A. Duta, S. Manolache, The influence of defects on the conduction in photoelectrodes used for water splitting, J. Optoelectron. Adv. Mater. 9 (2007) 1630.

[19] A. Enesca, A. Duta, J. Schoonman, Influence of tantalum dopant ions (Ta^{5+}) on the efficiency of the tungsten trioxide photoelectrode, Phys. Status Solidi (a) 205 (2008) 2038.

[20] S.B. Sadale, S.M. Chaqour, O. Gorochov, M. Neumann-Spallart, Photoelectrochemical and physical properties of tungsten trioxide films obtained by aerosol pyrolysis, Mater. Res. Bull. 43 (2008) 1472.

[21] J.M. Ortega, A.I. Martınez, D.R. Acosta, C.R. Maganaet, Structural and electrochemical studies of WO_3 films deposited by pulsed spray pyrolysis, Sol. Energy Mater. Sol. Cells 90 (2006) 2471.

[22] M. Regragui, M. Addou, A. Outzourhit, J.C. Bernéde, Elb. El Idrissi, E. Benseddik, A. Kachouane, Preparation and characterization of pyrolytic spray deposited electrochromic tungsten trioxide films, Thin Solid Films 358 (2000) 40.

[23] C. Matei Ghimbeu, R.C. van Landschoot, J. Schoonman, M. Lumbreras, Tungsten trioxide thin films prepared by electrostatic spray deposition technique, Thin Solid Films 515 (2007) 5498.

[24] A. Enesca, A. Duta, Tailoring WO_3 thin layers using spray pyrolysis technique, Phys. Status Solidi (c) 5 (2008) 3499.

[25] S. Asim, M. Radiman, M. Ambar bin Yarmo, Preparation of WO_3 nanoparticles using cetyl trimethyl ammonium bromide supermolecular template, Am. J. Appl. Sci. 6 (7) (2009) 1424.

[26] M. Deepa, A.K. Srivastava, S. Lauterbach, Govind, S.M. Shivaprasad, K.N. Sood, Electro-optical response of tungsten oxide thin film nanostructures processed by a template assisted electrodeposition route, Acta Mater. 55 (2007) 6095.

[27] W.H. Lai, J. Shieh, L.G. Teoh, I.M. Hung, C.S. Liao, M.H. Hon, Effect of copolymer and additive concentrations on the behaviors of mesoporous tungsten oxide, J. Alloys Compd. 396 (2005) 295.

[28] W.H. Lai, L.G. Teoh, Y.H. Su, J. Shieh, M.H. Hon, Hydrolysis reaction on the characterization of wormhole-like mesoporous tungsten oxide, J. Alloys Compd. 438 (2007) 247.

[29] W. Wang, Y. Pang, S.N.B. Hodgson, XRD studies of thermally stable mesoporous tungsten oxide synthesised by a templated sol–gel process from tungstic acid precursor, Micropor. Mesopor. Mater. 121 (2009) 121.

[30] J.H. Lei, D. Liu, L.P. Guo, X.M. Yan, H. Tong, Fabrication and characterization of hexagonal mesoporous silica monolith via post-synthesized hydrothermal process, J. Sol–Gel Sci. Technol. 39 (2006) 169.

[31] N. Asim, S. Radiman, M.A. Yarmo, Synthesis of WO_3 in nanoscale with the usage of sucrose ester microemulsion and CTAB micelle solution, Mater. Lett. 61 (2007) 2652.

[32] C. Vautier-Giongo, H.O. Pastore, Micellization of CTAB in the presence of silicate anions and the exchange between bromide and silicate at the micelle surface, J. Colloid Interface Sci. 299 (2006) 874.

[33] A. Jakubowska, Interactions of different counterions with cationic and anionic surfactants, J. Colloid Interface Sci. 346 (2010) 398.

[34] W. Li, M. Zhang, J. Zhang, Y. Han, Self-assembly of cetyltrimethylammonium bromide in ethanol–water mixtures, Front. Chem. China 4 (2006) 438.

[35] Z. Li, W.-T. Jiang, H. Hong, An FTIR investigation of hexadecyltrimethylammonium intercalation into rectorite, Spectrochim. Acta A 71 (2008) 1525.

[36] F. Daniel, B. Desbat, J.C. Lassegues, B. Gerand, M. Figlarz, Infrared and Raman study of WO_3 tungsten trioxides and WO_3, xH_2O tungsten trioxide hydrates, J. Solid State Chem. 67 (1987) 235.

[37] T. Ivanova, K.A. Gesheva, G. Popkirov, M. Ganchev, E. Tzvetkovaet, Electrochromic properties of atmospheric CVD MoO_3 and $MoO_{3\text{-}}WO_3$ films and their application in electrochromic devices, Mater. Sci. Eng. B 119 (2005) 232.

[38] B. Pecquenard, S. Castro-Garcia, J. Livage, P.Y. Zavalij, M.S. Whittingham, R. Thouvenotet, Structure of hydrated tungsten peroxides $[WO_2(O_2)H_2O]\cdot nH_2O$, Chem. Mater. 10 (1998) 1882.

[39] M. Deepa, M. Kar, S.A. Agnihotry, Electrodeposited tungsten oxide films: annealing effects on structure and electrochromic performance, Thin Solid Films 468 (2004) 32.

[40] R.A. Nyquist, Interpreting Infrared, Raman, and Nuclear Magnetic Resonance Spectra, vol. I. Variables in Data Interpretation of Infrared and Raman Spectra, Academic Press, 2001,, p. 3.

[41] M. Deepa, A.K. Srivastava, S.N. Sharma, Govind, S.M. Shivaprasad, Microstructural and electrochromic properties of tungsten oxide thin films produced by surfactant mediated electrodeposition, Appl. Surf. Sci. 254 (2008) 2342.

[42] B.G. Yacobi, Semiconductor Materials. An Introduction to Basic Principles, Kluwer Academic Publishers, New York, 2003, p. 117.

[43] T. He, J. Yao, Photochromism in composite and hybrid materials based on transition-metal oxides and polyoxometalates, Prog. Mater. Sci. 51 (2006) 810.

[44] A.Z. Moshfegh, R. Azimirad, O. Akhavan, Optical properties and surface morphology of evaporated $(WO_3)(1-x)$–$(Fe_2O_3)(x)$ thin films, Thin Solid Films 484 (2005) 124.

[45] R. Swanepoel, Determination of the thickness and optical constants of amorphous silicon, J. Phys. E 16 (1983) 1214.

[46] Z.Z. You, G.J. Hua, Refractive index, optical bandgap and oscillator parameters of organic films deposited by vacuum evaporation technique, Vacuum 83 (2009) 984.

[47] K. Muthu Karuppasamy, A. Subrahmanyam, Studies on the correlation between electrochromic colouration and the relative density of tungsten trioxide (WO_{3-x}) thin films prepared by electron beam evaporation, J. Phys. D: Appl. Phys. 42 (2009) 095301, doi:10.1088/0022-3727/42/9/095301.

[48] D.K. Madhup, D.P. Subedi, S.P. Chimouriy, Optical characterization and thickness estimation of Al^{3+} ion doped ZnO nano-films from transmittance spectra, J. Optoelectron. Adv. Mater. 12 (2010) 1035.

[49] F. Lai, M. Li, H. Wang, H. Hu, X. Wang, J.G. Hou, Y. Song, Y. Jiang, Optical scattering characteristic of annealed niobium oxide films, Thin Solid Films 488 (2005) 314.

[50] X. Wu, F. Lai, L. Lin, J. Lv, B. Zhuang, Q. Yan, Z. Huang, Optical inhomogeneity of ZnS films deposited by thermal evaporation, Appl. Surf. Sci. 254 (2008) 6455.

[51] K.J. Patel, C.J. Panchal, V.A. Kheraj, M.S. Desai, Growth, structural, electrical and optical properties of the thermally evaporated tungsten trioxide (WO_3) thin films, Mater. Chem. Phys. 114 (2009) 475.

[52] D.K. Owens, R.C. Wendt, Estimation of the surface free energy of polymers, J. Appl. Polym. Sci. 13 (1969) 1741.

[53] Z.Z. You, Combined AFM, XPS, and contact angle studies on treated indium–tin-oxide films for organic light-emitting devices, Mater. Lett. 61 (2007) 3809.

[54] S. Takeda, M. Fukawa, Y. Hayashi, K. Matsumoto, Surface OH group governing adsorption properties of metal oxide, Thin Solid Films 339 (1999) 220.

[55] M. Voinea, C. Vladuta, C. Bogatu, A. Duta, Surface properties of copper based cermet material, J. Mater. Sci. Eng. B 152 (2008) 76.